remote sensing

MDPI

Article

Improvement of High-Resolution Daytime Fog Detection Algorithm Using GEO-KOMPSAT-2A/Advanced Meteorological Imager Data with Optimization of Background Field and Threshold Values

Ji-Hye Han [1], Myoung-Seok Suh [1,*], Ha-Yeong Yu [1] and So-Hyeong Kim [2]

[1] Department of Atmospheric Science, Kongju National University, 56 Gongjudaehak-ro, Gongju-si 32588, Chungcheongnam-do, Republic of Korea; gihh1131@smail.kongju.ac.kr (J.-H.H.); hakkk96@smail.kongju.ac.kr (H.-Y.Y.)

[2] National Meteorological Satellite Center, Korea Meteorological Administration, 64-18 Guam-gil, Gwanghyewon-myeon, Jincheon-gun 27803, Chungcheongbuk-do, Republic of Korea; theod06@korea.kr

* Correspondence: sms416@kongju.ac.kr; Tel.: +82-41-850-8533

Abstract: This study aimed to improve the daytime fog detection algorithm GK2A_HR_FDA using the GEO-KOMPSAT-2A (GK2A) satellite by increasing the resolution (2 km to 500 m), improving predicted surface temperature by the numerical model, and optimizing some threshold values. GK2A_HR_FDA uses numerical model prediction temperature to distinguish between fog and low clouds and evaluates the fog detection level using ground observation visibility data. To correct the errors of the numerical model prediction temperature, a dynamic bias correction (DBC) technique was developed that reflects the geographic location, time, and altitude in real time. As the numerical model prediction temperature was significantly improved after DBC application, the fog detection level improved (FAR: −0.02–−0.06; bias: −0.07–−0.23) regardless of the training and validation cases and validation method. In most cases, the fog detection level was improved due to DBC and threshold adjustment. Still, the detection level was abnormally low in some cases due to background reflectance problems caused by cloud shadow effects and navigation errors. As a result of removing navigation errors and cloud shadow effects, the fog detection level was greatly improved. Therefore, it is necessary to improve navigation accuracy and develop removal techniques for cloud shadows to improve fog detection levels.

Keywords: fog; fog detection algorithm; GEO-KOMPSAT-2A (GK2A); bias correction; visibility meter; cloud shadow; navigation error

Citation: Han, J.-H.; Suh, M.-S.; Yu, H.-Y.; Kim, S.-H. Improvement of High-Resolution Daytime Fog Detection Algorithm Using GEO-KOMPSAT-2A/Advanced Meteorological Imager Data with Optimization of Background Field and Threshold Values. *Remote Sens.* **2024**, *16*, 2031. https://doi.org/10.3390/rs16112031

Academic Editor: Filomena Romano

Received: 7 May 2024
Revised: 3 June 2024
Accepted: 3 June 2024
Published: 5 June 2024

1. Introduction

Fog is a phenomenon in which small-sized (5 to 20 μm) water droplets or supercooled water droplets float in the atmosphere and form a layer in contact with the ground with a horizontal visibility of less than 1 km [1]. Fog not only affects visibility, but also directly affects human activities such as land, air, and maritime transportation through reduced visibility [2–5]. Therefore, improving fog detection and prediction is essential for reducing human and economic losses caused by fog [6].

Due to the localized properties of fog generation and dissipation processes, most studies were conducted to statistically characterize and classify fog types using ground observation data [7–11]. However, ground observation data have disadvantages such as uneven distribution of observation points, limitations in spatial representativeness, and limitations in observation elements [2,3,12]. Also, continuous calibration and quality control are required because the visibility system includes errors depending on the measurement method [13]. Recently, to solve these problems with ground observation data, studies

have been conducted using satellites to detect fog where it is difficult to install observation equipment, such as the sea and mountainous areas [14–17].

Fog detection techniques using satellites have been developed based on the optical and physical characteristics of fog [14–18]. Methods using dual channel difference (DCD) or reflectance, which are commonly used to detect fog, are effective in distinguishing between fog and clear areas or mid-to-upper-level clouds but have difficulty distinguishing between deserts, snow areas, low-level clouds, and semi-transparent cirrus clouds [14,15]. Bendix et al. [16] used the brightness temperature difference (BTD) between the 11.77 μm and 12.27 μm channels to remove mid-to-upper-level clouds that are misidentified as fog, and Cermark [18] utilized the normalized difference snow index (NDSI), using the 1.6 μm and 0.6 μm channels, to remove snow-covered areas that have similar reflectivity to fog. Gultepe et al. [19] attempted to distinguish between fog and low-level clouds using the temperature and relative humidity (RH) of the global environmental multiscale (GEM) model. Musial et al. [20] utilized a 5 × 5 kernel method based on the difference in surface roughness between fog and clouds to remove misidentified pixels at the edges of clouds. Shang et al. [17] attempted fog detection using wavelengths such as 0.86 μm, 1.6 μm, 2.3 μm, and 7.3 μm, which were previously unused in conventional geostationary meteorological satellites, with the Himawari-8/AHI (Advanced Himawari Imager) in Japan. Egle et al. [3] and Weston and Temimi [21] attempted fog detection using machine learning and the pseudo-emissivity method, respectively. Thus, various methods are being developed worldwide to improve fog detection levels.

In South Korea, many researchers have also conducted fog detection using satellites to reduce the damage caused by fog. Park and Kim [12], Shin et al. [22], and Suh et al. [23] utilized the local standard deviation (LSD) of the infrared channel and sea surface temperature to improve the fog detection level using DCD or reflectivity. Recently, with the launch of geostationary satellites such as Himawari-8/AHI and GK2A (GEO-KOMPSAT-2A)/AMI (Advanced Meteorological Imager), which have significantly improved performances, there have been studies attempting high-resolution fog detection using various channels compared to conventional geostationary satellites (e.g., COMS: Communication, Ocean, and Meteorological Satellite) [24–27]. Han et al. [27] used GK2A/AMI data, which has greatly improved observation performance in terms of the number of channels and spatiotemporal resolution. They developed a fog detection algorithm (GK2A_FDA) using a total of nine algorithms according to geographical location (land/coast/sea) and time (day/night/dawn). GK2A_FDA showed a high fog detection level (probability of detection (POD) of 0.7 or higher) regardless of time, space, and fog case. Still, it exhibited an over-detection of fog (bias greater than 1). In particular, the fog detection level was low during the daytime regardless of the geographical location or fog case.

Therefore, in this study, to improve the fog detection level during the day using GK2A/AMI, we (1) increased the resolution of fog detection (from 2 km to 500 m, 16 times), (2) improved the surface temperature fields predicted by numerical models, and (3) optimized some thresholds. Section 2 introduces the data and improvements in fog detection methods used in the 500 m resolution fog detection algorithm. Section 3 qualitatively and quantitatively presents the fog detection levels according to geographical location and fog case. Sections 4 and 5 discuss the limitations of the GK2A fog detection algorithm and summarize the research findings obtained in this study, respectively.

2. Materials and Methods

2.1. Materials

In this study, to improve the fog detection algorithm and validate the fog detection level of the high-resolution fog detection algorithm using GK2A (GK2A_HR_FDA), (1) GK2A/AMI, (2) dynamic auxiliary data such as surface temperature data predicted by numerical models, and (3) ground observation data such as visibility meter were used. The GK2A/AMI provided by the National Meteorological Satellite Center (NMSC), a geostationary satellite in operational use since July 2019, observes the full-disk area at

10 min intervals [28,29]. The center wavelengths and spatial resolutions of GK2A/AMI used in this study are listed in Table 1. GK2A/AMI is equipped with 16 channels, including 12 infrared channels and 4 visible channels [30]. The spatial resolution of the infrared channels is 2 km, and most visible channels have a spatial resolution of 1 km [26,29]. However, the visible channel 3 (VIS0.6) observes the full-disk area at a spatial resolution of 500 m [26,29]. Among the 16 channels, we used 8 channels and attempted local fog detection using visible channel 3, which has the highest resolution (500 m). The other seven channels were used as an auxiliary to differentiate fog from snow cover, low-level clouds, and semi-transparent cirrus clouds, which are difficult to distinguish through visible channels alone.

Table 1. Summary of satellite data used for the daytime fog detection algorithm.

Channel	AMI Band	Central Wavelength [μm]	Spatial Resolution [km]	Usage
1	VIS0.4	0.470	1	-
2	VIS0.5	0.511	1	-
3	VIS0.6	0.640	0.5	O
4	VIS0.8	0.856	1	-
5	NIR [1] 1.3	1.374	2	-
6	NIR1.6	1.610		O
7	IR [2] 3.8	3.830		O
8	WV [3] 6.2	6.241		-
9	WV6.9	6.952		-
10	WV7.3	7.344		-
11	IR8.7	8.592		O
12	IR9.6	9.625		-
13	IR10.5	10.403		O
14	IR11.2	11.212		O
15	IR12.3	12.364		O
16	IR13.3	13.310		O

[1] NIR: near infrared channel; [2] IR: infrared channel; [3] WV: water vapor channel.

GK2A_HR_FDA primarily detects fog using the reflectance difference. However, reflectance of 0.64 μm ($R_{0.64}$) is influenced by the solar zenith angle (SZA). Therefore, we used the background field of clear sky reflectance ($Clr\_SFC\_R_{0.64}$) produced by the 30-day minimum value composite method (mVC) to minimize this effect. To distinguish fog from clouds such as low clouds, we used clear sky radiance (CSR) provided by the NMSC as a background ground temperature field simulated by RTTOV12.3 (the radiative transfer for TIROS operational vertical sounder version 12.3), utilizing the vertical profile of temperature and humidity from the united model (UM). The CSR is calculated with a resolution of 10 km every hour.

Due to the difference in spatiotemporal resolution between the numerical model and the GK2A/AMI, the spatiotemporal resolution of the numerical model was interpolated to 10 min and 500 m. Additionally, snow cover, cloud mask, and fog product from a previous time were used as dynamic auxiliary data. As static auxiliary data, we utilized the land–sea mask, land cover, and threshold look-up table.

For the validation data, we used visibility meter data provided by the Korea Meteorological Administration (KMA), selecting approximately 180 locations known for their excellent quality out of around 280 visibility meter datasets (Figure 1). And the visibility data observed at seven airports were used. To partially resolve quality issues with visibility data, we used RH and wind speed (WS) observed by the automatic weather system (AWS). The visibility meter and AWS, which observe at 1 min intervals, were colocated by the moving average of a 10 min period.

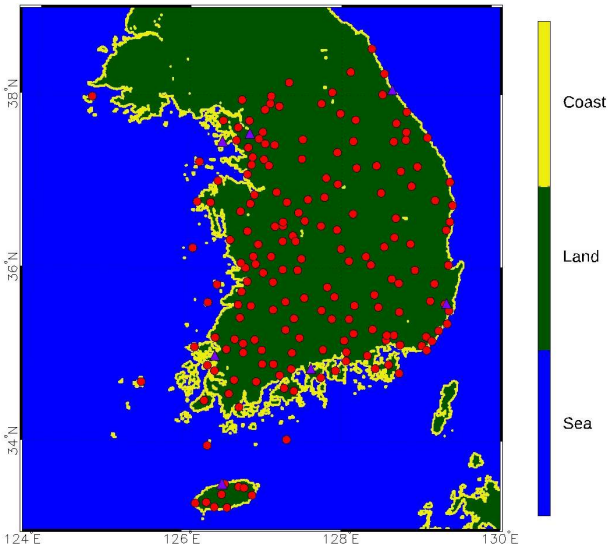

Figure 1. Spatial distribution of ground observation station visibility meter (AWS/ASOS) with land–sea mask with 500 m resolution and 7 airports (Incheon, Gimpo, Jeju, Ulsan, Muan, Yeosu, and Yangyang). The red circle symbolizes the AWS/ASOS and the purple triangle symbolizes the airport.

For the development and validation of fog detection algorithms, 32 fog cases around the Korean Peninsula were used as training cases (T1–T20) and validation cases (V1–V12), as shown in Table 2. To reflect the fact that fog generation characteristics differ depending on the season, we selected 20 training cases (5 for each season) and 12 validation cases (3 for each season). Additionally, to evaluate the level of fog detection according to the intensity of the fog, we selected various cases with weak and strong intensities.

Table 2. List of 32 fog cases selected for the daytime fog detection algorithm (T# and V# stand for the training cases and validation cases, respectively).

Code	MAM	# of Fog [1]	Code	JJA	# of Fog	Code	SON	# of Fog	Code	DJF	# of Fog
T1	03.01.20	139	T6	07.26.19	82	T11	09.24.19	304	T16	12.08.19	127
T2	03.05.21	525	T7	08.25.19	73	T12	09.29.19	327	T17	12.28.20	501
T3	03.08.21	223	T8	08.26.19	137	T13	10.04.19	326	T18	01.24.21	97
T4	03.14.21	422	T9	08.30.19	247	T14	10.20.19	717	T19	02.07.21	404
T5	03.25.21	96	T10	08.31.19	42	T15	11.06.19	553	T20	02.13.21	113
V1	04.17.21	205	V4	06.06.21	27	V7	09.30.19	354	V10	12.11.19	106
V2	05.03.21	106	V5	06.12.21	100	V8	11.05.19	498	V11	02.13.20	124
V3	05.19.21	258	V6	06.19.21	82	V9	11.12.19	271	V12	12.08.21	254

[1] # of fog refers to the number of times fog was observed at all visibility observatories.

2.2. Methods

2.2.1. GK2A High-Resolution Fog Detection Algorithm

Figure 2 shows the flowchart of the GK2A_HR_FDA, developed for daytime fog detection using GK2A/AMI data. The GK2A_HR_FDA comprises two primary phases: an offline algorithm development process and an online real-time fog detection process. During algorithm development, test elements for fog detection are selected based on the optical and textural characteristics of fog, and thresholds are optimized. This study aimed to enhance the algorithm (referred to as GK2A_FDA) that is currently operational at the NMSC. The detailed explanations about the GK2A_FDA can be found in Han et al. [27]. So, we will briefly introduce the GK2A_FDA and focus on detailing the improvements made.

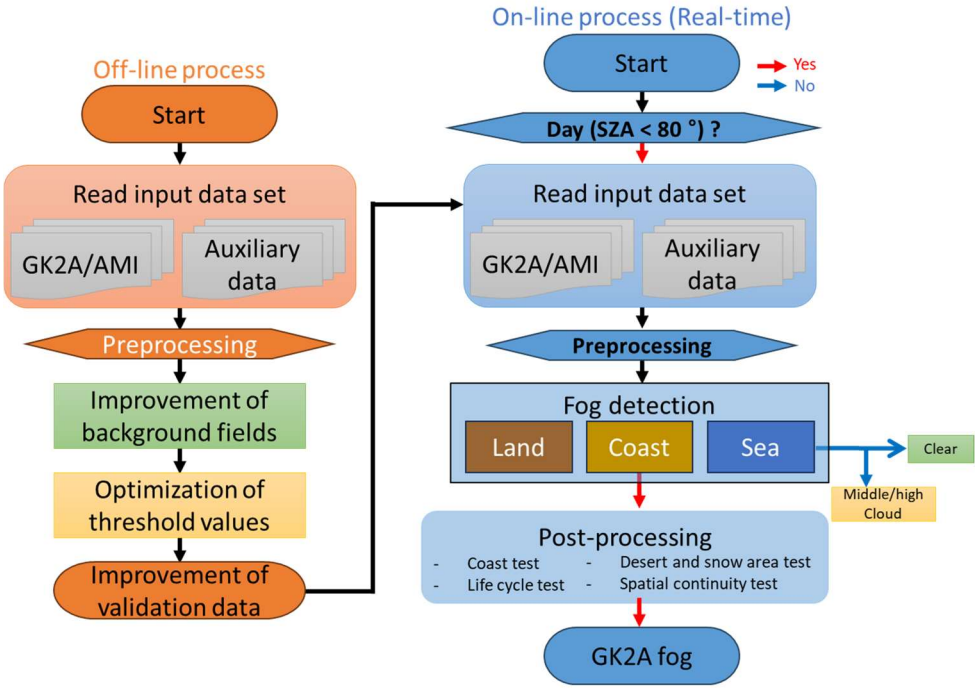

Figure 2. Flow chart of GK2A high-resolution fog detection algorithm operating in daytime.

The GK2A_FDA utilizes a decision tree method based on the optical and textural properties of fog. GK2A_FDA consists of nine algorithms based on the time of application (day, night, and dawn/sunset) and geographic location (land, sea, and coast). At night, the DCD, temperature difference between the shortwave infrared channel and the infrared channel, was mainly used. During the day, ΔVIS, the difference between the 0.64 μm reflectance and $Clr\_SFC\_R_{0.64}$, was mainly used. The nighttime fog detection algorithm consisted of five steps, including a DCD test, the difference between fog top temperature and surface temperature (ΔFTs) test, the LSD test, etc. During the daytime, eight fog detection steps were used, including calculating the ΔVIS test, ΔFTs test, normalized LSD (NLSD) test, and the BTD test, among others. To minimize temporal discontinuity at dawn, previous fog detection results were utilized, and the other three tests were performed to detect newly generated fog or remove falsely detected cloud pixels. In addition, to consider the spatial continuity of fog, the results of the land fog algorithm and the sea fog algorithm were blended for coastal regions. The final products of GK2A_FDA are a 2 km spatial resolution fog detection result and a quality flag.

The GK2A_HR_FDA algorithm developed in this study is based on a decision tree method. The threshold values used in GK2A_FDA were utilized as the initial thresholds. By slightly adjusting these initial thresholds, the fog detection level for the 20 training fog cases is validated, and the threshold yielding the best detection level based on the Hanssen–Kuiper Skill Score (KSS) is considered the optimized threshold.

The GK2A_HR_FDA detects fog by initially assuming that all pixels are fog and then removing non-fog pixels at each detection step. Table 3 summarizes the test elements of GK2A_HR_FDA and thresholds for each step and geographical location. Initially, we used a method of discriminating clear pixels at a 500 m resolution to remove pixels that were less likely to have fog.

This discrimination was achieved by calculating the difference between the 0.64 μm reflectance and $Clr\_SFC\_R_{0.64}$. Subsequently, to distinguish low-level clouds, snow cover, and some high-reflectance pixels that are difficult to differentiate from fog based solely on reflectance, an additional test was conducted. This test consisted of 10 levels on land and 7 levels on sea.

Table 3. Definition and threshold of each test element used in GK2A_HR_FDA.

Step	Test Element	Definition	Threshold	Category	SFC Type	
Start				All fog	L	S
1	ΔVIS	$R_{0.64} - Clr\_SFC\_R_{0.64}$	<3.0%	Clear	O	O
2	ΔFTs	$BT_{11.2} - DBC\_CSR\_BT_{11.2}$	<−4.25 K >1.0 K	Cloud Clear	O	O
3	NLSD_VIS	$\frac{\text{SD of 3 } \times \text{ 3 pixels}}{\text{Ave. of 3 } \times \text{ 3 pixels}}$	≥0.2	Unknown	O	O
4	BTD1	$BT_{13.3} - BT_{11.2}$	<−19.0 K	Clear	O	O
5	NDSI	$\frac{R_{0.64} - R_{1.6}}{R_{0.64} + R_{1.6}}$	<−0.15 >0.4	Clear Snow	O	-
6	BTD2	$BT_{10.5} - BT_{12.3}$	>4.0 K	Cloud	O	O
7	BTD3	$BT_{8.7} - BT_{11.2}$	>−1.3 K	Clear	O	O
8	Strict threshold test		ΔVIS > 4.0% ΔFTs > −4.0 K NLSD_VIS < 0.1	Fog (else Unknown)	O	-
9	DCD	$BT_{3.8} - BT_{11.2}$	$f(SZA)$	Unknown	O	O
10	ΔDCD	DCD(t) − DCD(t − 1)	−0.14 < ΔDCD < 0.35	Unknown	O	-

2.2.2. Dynamic Bias Correction

As seen in Figure 3, to minimize the false detection of low-level clouds as fog, the accuracy of the background data (brightness temperature (BT) of CSR for the 11.2 μm channel, referred to as $CST\_BT_{11.2}$) used in the second step (ΔFTs test) is crucial [19]. In particular, in the ΔFTs test, it can be observed that POD decreased sharply while FAR remained relatively unchanged compared to other test elements. As is well known, the reason for the rapid decrease in POD is that the predictive performance of numerical models is affected by geographic location, season, time, weather, etc. [31–33]. Therefore, in this study, to improve the accuracy of $CSR\_BT_{11.2}$, simple distance interpolation followed by altitude correction was performed.

$$\Delta h_{i,j} = h_{i,j} - nwp\_h_{i,j}, \tag{1}$$

where $h_{i,j}$ is the altitude data (digital elevation model, DEM) obtained from the NMSC with a resolution of 500 m. $nwp\_h_{i,j}$ is the altitude of the numerical model interpolated to a resolution of 500 m. $\Delta h_{i,j}$ is the difference between $h_{i,j}$ and $nwp\_h_{i,j}$.

$$CSR\_BT_{11.2i,j}(L) = CSR\_BT_{11.2i,j}(L) - \frac{0.65\ K}{100\ m} \times \Delta h_{i,j}, \tag{2}$$

where L represents land. In contrast to land, where altitude variability is absent, interpolation was only based on the distance on the sea. Considering the predictive characteristics of numerical models, we developed a dynamic bias correction (DBC) method that allows for correction every 10 min based on the geographical location (land, sea, and coast)—Equations (3) to (6) represent the DBC process sequentially. To calculate the bias of the numerical model for each geographical location, as shown in Equation (3), we calculated the deviation using all clear pixels identified in the cloud mask provided by the NMSC and analyzed the distribution of these deviations.

$$dev_{i,j}(ls) = CSR\_BT_{11.2i,j}(ls) - BT_{11.2\ i,j}(ls), \tag{3}$$

where $dev_{i,j}$ means the deviation between $CSR\_BT_{11.2i,j}$ and BT for the 11.2 μm channel ($BT_{11.2i,j}$), and ls indicates the geographical location classified as land (L), sea (S), or coast (C). When $dev_{i,j}$ values were abnormally high, those pixels exhibited a high reflectance like that of clouds, thus resulting in the misclassification of those pixels as clear when they were cloud pixels. In this study, to minimize errors in the cloud mask, we excluded pixels from clear pixels if $dev_{i,j}$ exceeded $\pm 1.5\sigma(ls)$ compared to mean of $dev_{i,j}(ls)$ (Equation (4)).

After mitigating the influence of clouds, we calculated the mean bias for each surface type using Equation (5).

$$\sigma(ls) = \sqrt{\frac{1}{n}\sum_{1}^{n}\left(dev_{i,j}(ls) - mean\_dev(ls)\right)^2}, \tag{4}$$

$$\begin{aligned} bais(ls) &= \frac{1}{m}\sum_{1}^{m} dev_{i,j}(ls) \\ bias(C) &= \frac{bias(L)+bias(S)}{2}, \end{aligned} \tag{5}$$

where n is the total number of clear pixels for both land and sea and *mean_dev* signifies the average deviation. m denotes the number of clear pixels after excluding outliers with a deviation greater than $\pm 1.5\sigma(ls)$. Since it is difficult to obtain enough clear pixels every 10 min in the coastal region, the biases for land and sea are averaged to minimize spatial discontinuity between land and sea.

$$DBC\_CSR\_BT_{11.2i,j}(ls) = CSR\_BT_{11.2i,j}(ls) - bias(ls), \tag{6}$$

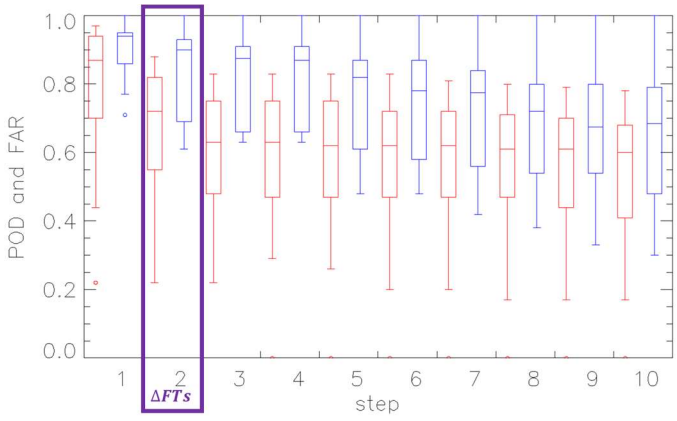

Figure 3. Variation in POD and FAR according to the fog detection steps for the selected 20 fog training cases. Red and blue colored bars stand for the POD and FAR, respectively. Red and blue circles indicate exceptionally low POD and FAR.

Finally, the ΔFTs was defined using the $DBC\_CSR\_BT_{11.2}$ obtained from Equation (6), as presented in Table 3. DBC is a method for correcting model errors based on geographical location and time, irrespective of the type of numerical model. Therefore, it can be applied even if the model data are changed in the future.

2.2.3. Validation

To analyze the qualitative fog detection level of GK2A_HR_FDA, we compared and analyzed the spatial distribution of fog detection data from GK2A_HR_FDA with visible channel images and visibility data. Statistical validation was performed using ground observation data for the quantitative analysis of fog detection levels. Visibility data were primarily used to define fog and non-fog conditions among the ground observation data. To minimize spatial representativeness and measurement errors inherent in visibility data, fog or non-fog conditions were redefined for observation points with visibility within 2 km using RH and WS (Table 4). First, if the RH was less than 88%, the fog was redefined as non-fog even if the visibility was less than 1 km [30,34]. Radiation fog primarily occurs when the wind is weak, while upslope fog or advection fog, such as sea fog, occurs when the wind blows [8]. Therefore, the fog was redefined as non-fog using WS only in inland areas, and the threshold values were referenced from Lee and Suh [35] and Kim et al. [36]. On the other hand, for non-fog stations with visibility between 1 and 2 km, non-fog was redefined as fog based on the frequency analysis of RH and WS according to visibility. In

this case, the threshold for WS was set more strictly compared to when the visibility was less than 1 km.

Table 4. Sophistication of ground observed visibility data using relative humidity (RH) and wind speed (WS) according to geographic location.

Visibility [km]	RH [%]	WS [m/s]	Land–Sea Mask	Observation Fog
<1	≥88	<2.5	Land/Coast	Fog
		≥2.5	Land	Non-fog
			Coast	Fog
	<88	-	Land/Coast	Non-fog
	No data		Land/Coast	Fog
1–2	≥98	<1.5	Land/Coast	Fog
		≥1.5	Land	Non-fog
			Coast	Fog
	No data		Land/Coast	Non-fog
≥2	-	-	Land/Coast	Non-fog

The differing observation frequencies between ground observation data and satellite data were colocated by averaging the ground observation data over 10 min, and spatial colocation was performed by using the nearest satellite pixels to the ground observation data. In the validation process, a method using the surrounding 3 × 3 pixels (1:9 validation method: 1:9 vali.), as proposed by Cermak et al. [18], was also employed to minimize satellite navigation errors. Table 5 presents a 2 × 2 contingency table for statistical validation using both the nearest pixel method (1:1 validation method: 1 vali.) and the 1:9 validation method. In the 1:9 validation method, the fog (or non-fog) status was determined based on the fog detection results of the surrounding 3 × 3 pixels in the GK2A_HR_FDA output. The 1:9 validation method uses how many of the surrounding 3 × 3 pixels in the GK2A_HR_FDA result are fog (or non-fog). When the ground observation data indicated fog, a hit was recorded if any of the 9 pixels in the GK2A_HR_FDA output detected fog. Conversely, it was classified as a miss if no fog was detected in any of the 9 pixels in the GK2A_HR_FDA output. When the ground observation data indicated non-fog conditions, if 5 or more of the 9 pixels in the GK2A_HR_FDA output were classified as fog, it was defined as a false alarm, while if fewer than 5 pixels were classified as fog, it was considered a correct negative.

Table 5. Contingency table according to the validation method: use of pixels closest to the ground observation point (1:1 validation method: 1:1 vali.) and use of adjacent 3 × 3 pixels (1:9 validation method: 1:9 vali.).

GK2A_HR_FDA		Observation Fog		
Nearest satellite pixel (1:1 vali.)	Fog Non-fog	Fog Hit (H) Miss (M)	Fog Non-fog	Non-fog False alarm (F) Correct negative (C)
# of fog pixel for 3 × 3 pixels (1:9 vali.)	≥1 =0	Hit (H) Miss (M)	≥5 <5	False alarm (F) Correct negative (C)

The statistical validation indices for evaluating the detection performance of GK2A_HR_FDA are given by Equations (7) to (10).

$$\mathrm{POD} = \mathrm{H}/(\mathrm{H} + \mathrm{M}), \tag{7}$$

$$\mathrm{FAR} = \mathrm{F}/(\mathrm{H} + \mathrm{F}), \tag{8}$$

$$\mathrm{Bias} = (\mathrm{H} + \mathrm{F})/(\mathrm{H} + \mathrm{M}), \tag{9}$$

$$CSI = H/(H + F + M), \quad (10)$$

POD and the critical success index (CSI) represent the proportion of successful fog detections by GK2A_HR_FDA, with values closer to 1 indicating a better fog detection performance. A smaller false alarm ratio (FAR), which is the rate of false detections, corresponds to a better fog detection performance. Bias, which is the degree of bias in fog detection results, signifies over-detection if it is greater than 1 and under-detection if it is less than 1.

3. Results

3.1. Result of Dynamic Bias Correction

Figure 4 shows the bias of the numerical model and the results of DBC according to the geographical location and time (10 min intervals) for 20 selected training cases. Negative biases were predominantly observed over land. While the magnitude of the bias varied depending on time and date, it consistently exhibited a diurnal variation regardless of the specific date. Negative biases were prominent during daytime with high solar elevation angles (10–14 KST; Korea standard time), necessitating bias adjustments over time through DBC. To detail spatial changes in temperature depending on the terrain on land, bias corrections were made after adjusting for altitude effects. Even though numerical model predictions, accounting for altitude effects, and more accurately depict spatial variations attributed to terrain, the bias remains relatively unchanged before and after accounting for altitude effects (Figure 4a,b). This suggests that the spatial averaging of altitude differences between numerical models and satellite data offsets differing altitude effects based on geographical location. Post-DBC application, the bias of the numerical model tended to approach zero regardless of the date and time. In contrast, predominantly positive biases were observed over the sea, smaller than those over land. Despite varying with time and the case, biases over the sea generally decreased after DBC application across most cases. Reductions in bias after DBC could also be observed along the coast.

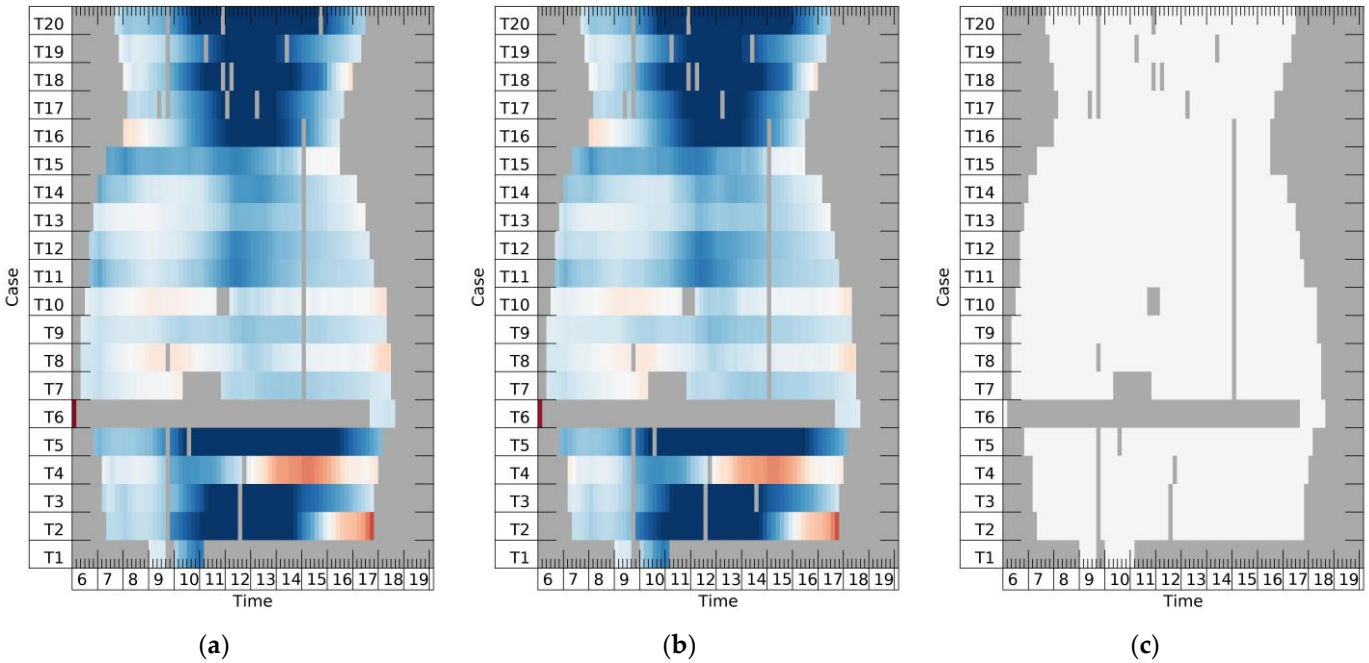

Figure 4. *Cont.*

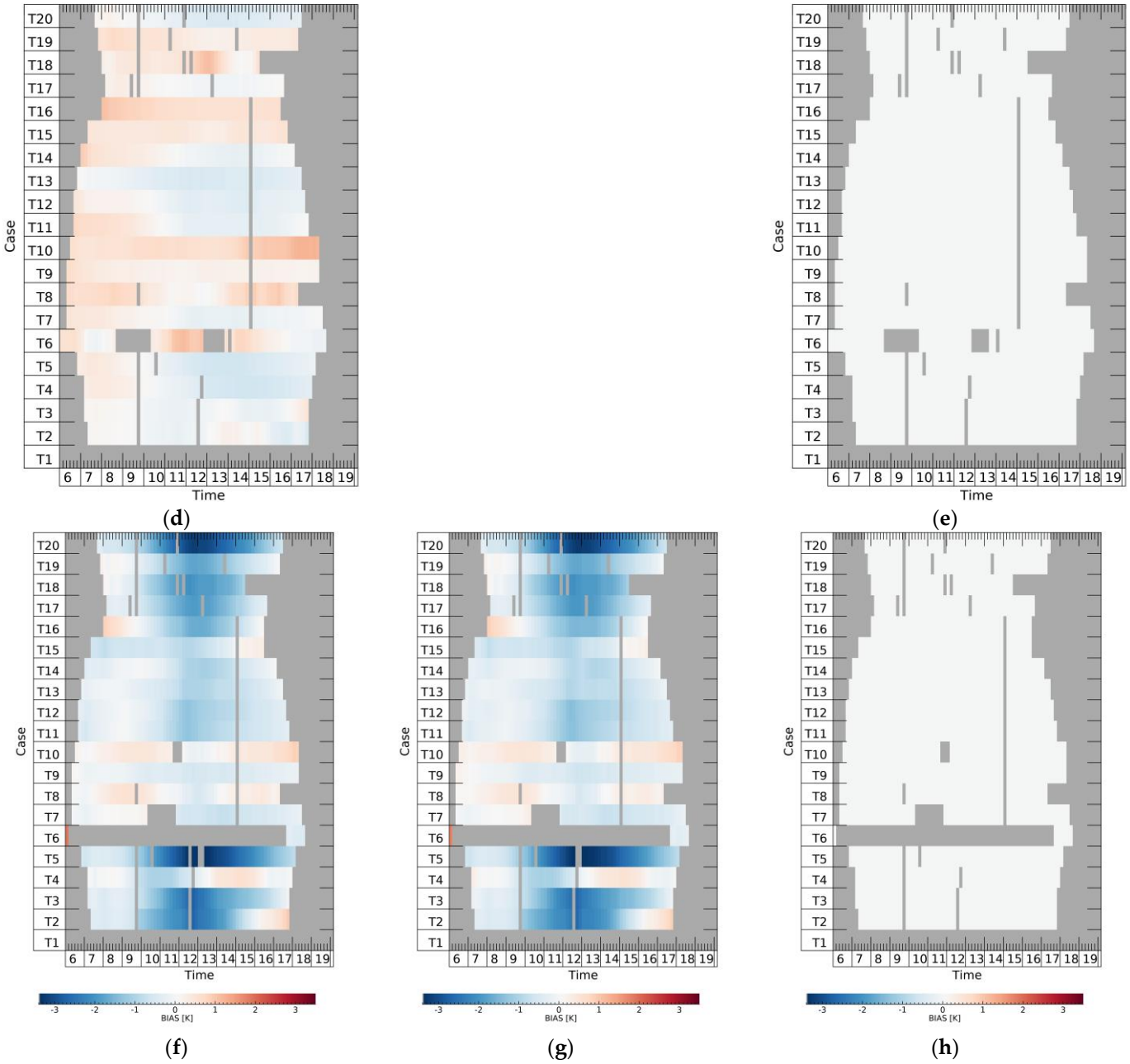

Figure 4. Distribution of average ground temperature deviation (K) by interpolation method of numerical model data, geographic location (land/sea/coast), and time (10 min intervals). (**a**,**d**,**f**) Biases of simple distance interpolation for land, sea, and coast, respectively. (**b**,**g**) Bias after considering the topography effect. (**c**,**e**,**h**) Biases after performing dynamic bias correction. T# on the vertical axis represents the fog cases presented in Table 2.

3.2. Qualitative Fog Detection Results of GK2A_HR_FDA

Figure 5 shows the fog detection results of GK2A_HR_FDA, along with visible channel imagery and surface observational data. Figure 5a,b depict cases of heavy fog occurring throughout South Korea, with low-level clouds passing over the southern coast. GK2A_HR_FDA effectively detected fog from inland areas, which aligns with regions of high reflectance in the visible imagery. Also, the fog pixels in GK2A_HR_FDA matched well with the stations where fog appears in the spatial distribution of ground observations. While distinguishing low-level clouds along the southern coast from fog, some misclassifications occurred near the edges of these clouds. Around 37°N, areas with high reflectance observed

as non-fog in ground observations were falsely detected as fog by GK2A_HR_FDA. This problem, caused by the dissipation characteristics of radiation fog after sunrise, is a limitation of validation using ground observation data [24]. As the boundary layer temperature rises due to land surface heating, fog dissipates from its lower layers, leading to continued fog detection from satellites but observation of non-fog conditions on the surface.

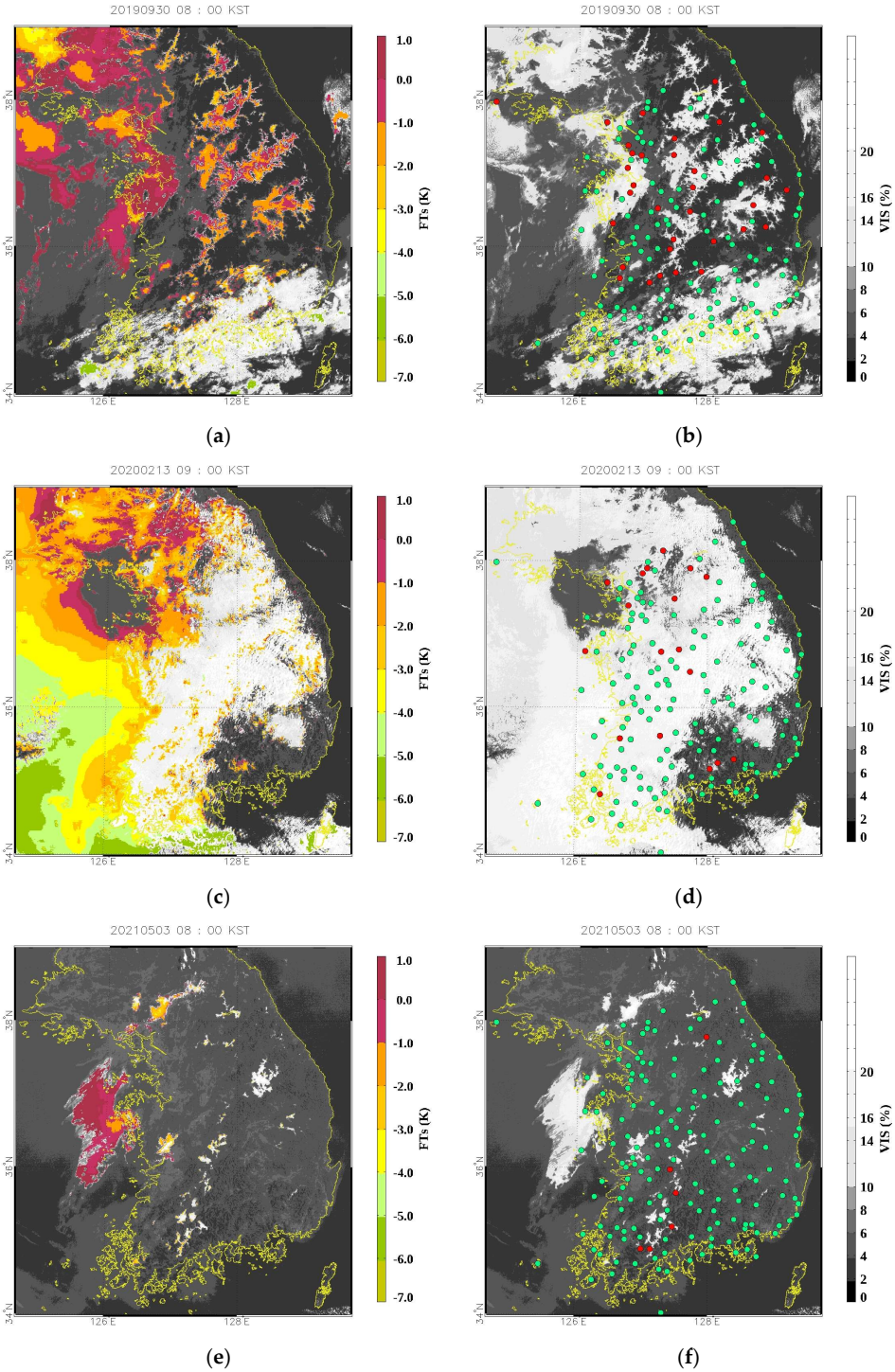

Figure 5. Sample images of fog detection results (**a**,**c**,**e**) and ground fog data (**b**,**d**,**f**) with visible images of 0.64 μm channel (red and green circles represent foggy and non-foggy area classified by visibility meter data, respectively). (**a**,**b**) Strong fog cases at 08:00 KST on 30 September 2019. (**c**,**d**) Cases of fog with low cloud at 09:00 KST on 13 February 2020. (**e**,**f**) Weakly occurring fog cases at 08:00 KST on 3 May 2021.

Figure 5c,d are cases of widespread sea fog in the western sea. Some observation stations may have observed fog, but low-level clouds appeared inland when visible images were animated. GK2A_HR_FDA effectively detected widespread sea fog. Compared to the observation station that observed fog occurring along the coast, GK2A_HR_FDA effectively detected coastal fog. It also effectively detected locally occurring fog near 35°N and 128°E. However, there were still false-detected pixels at the edges of the clouds. This problem persisted despite the improved accuracy of the background data. Some fogs observed inland could not be detected. These observation stations are cases where fog occurred under low-level clouds, which is a limitation of fog detection using meteorological satellites.

Figure 5e,f show cases where fog occurred very locally with weak intensity. When the visible imagery was animated, fog could be observed over the Yellow Sea. GK2A_HR_FDA was good at detecting fog areas observed in ground observation data as fog pixels. It also detected sea fog well, except for some edges. As in the previous case, some pixels were falsely detected due to differences between ground observation data and satellite data during fog dissipation.

3.3. Quantitative Fog Detection Results of GK2A_HR_FDA

This study applied DBC to GK2A_HR_FDA, and the ΔFTs threshold was reoptimized using 20 training cases. The threshold was optimized by incrementally increasing around the existing threshold (−3.50 K) by intervals of 0.25 K. The optimized threshold was determined comprehensively, evaluating the KSS and bias. The optimized threshold changed from −3.50 K to −4.25 K, which appeared to result from correcting negative biases in the DBC process (Figure 4). The fog detection results using this optimized threshold are summarized for both training and validation cases in Table 6.

Table 6. Summary of quantitative validation of fog detection results before and after applying dynamic bias correction.

Validation Method		20 Training Cases				12 Validation Cases			
		1:9 Vali.		1:1 Vali.		1:9 Vali.		1:1 Vali.	
		Before	After	Before	After	Before	After	Before	After
POD	Mean	0.74	0.75	0.60	0.61	0.66	0.65	0.50	0.48
	SD	0.13	0.13	0.15	0.14	0.15	0.16	0.16	0.17
FAR	Mean	0.59	0.56	0.65	0.63	0.62	0.56	0.69	0.65
	SD	0.20	0.21	0.17	0.17	0.27	0.28	0.24	0.25
Bias	Mean	1.79	1.71	1.70	1.63	1.71	1.49	1.61	1.38
	SD	1.42	1.25	1.39	1.21	2.45	2.59	2.53	2.67
CSI	Mean	0.36	0.38	0.29	0.30	0.32	0.35	0.24	0.26
	SD	0.14	0.15	0.11	0.11	0.20	0.20	0.15	0.14

For the training case, the improvement in the accuracy of the background data increased POD and CSI by 0.01–0.02, and decreased FAR by 0.02–0.03, regardless of the validation method. Using the 1:9 validation method, the bias decreased from 1.79 to 1.71, and using the 1:1 validation method, it decreased from 1.70 to 1.63, partially resolving the over-detection tendencies. Although there were differences depending on the validation method, POD increased and FAR decreased after DBC application, and the bias approached 1.0, indicating that the fog detection level of GK2A_HR_FDA was improved.

The standard deviation (SD) for each validation index remained mostly unchanged; there was a slight decrease of about 0.06 in the bias, indicating an improvement in fog detection level after DBC in terms of stability.

For the validation case, the reduction in FAR (−0.06) was more significant than that in POD (−0.01) using the 1:9 validation method; in addition, POD decreased by 0.02 using the 1:1 validation method, but FAR and bias decreased by 0.04 and 0.23, respectively. The fact that the bias approached 1.0 regardless of the validation method indicates that the detection level of GK2A_HR_FDA was also improved in the validation cases.

The SD either remained the same or decreased, suggesting that the improved accuracy of the background data influenced the fog detection results. Therefore, it can be inferred that the improvement in the background data accuracy contributed to the overall enhancement in the accuracy of GK2A_HR_FDA regardless of the validation method or case.

The fog detection level was evaluated based on the geographical location, considering differences in fog occurrence characteristics and background conditions. When validated using a 1:9 validation method, the average POD on the coast (0.81) was higher than on land (0.64). Conversely, the average FAR was much higher on the coast (0.86) compared to land (0.46). Regardless of geographic location, GK2A_HR_FDA tended to over-detect (bias > 1), especially on the coast, with a significant over-detection of 5.71. It can be seen that the level of fog detection according to geographical location was significantly higher on land. This is because most fog pixels used in the overall validation were land fog pixels (about 90%). At the coast, the SD of the bias was very large regardless of the fog case and validation method. This large SD of the bias means that the level of fog detection at the coast varied greatly depending on the case, so the stability of fog detection at the coast needs to be improved.

Figure 6 presents the detection levels according to the validation method (1:1 vali. and 1:9 vali.) and for each fog case using a performance diagram. In the performance diagram, the top-right corner signifies the highest detection level, while the bottom-left indicates the lowest. The red diagonal line connecting the top left to the bottom right represents where POD equals FAR, and positioned above this diagonal suggests a good detection level. Regardless of the fog case, the fog detection levels were higher with the 1:9 validation method compared to the 1:1 validation method. The fog detection results varied significantly depending on the validation method and fog case.

The high POD, CSI, and success rate (1-FAR) values using the 1:9 validation method suggested that fog detection levels were very good (Figure 6a). Moreover, uncertainty is low when fog detection levels are high. In T14, where the most fog occurred, the fog detection level was the best, with a POD of 0.76 and FAR of 0.32 using the 1:1 validation method (Figure 6b). Most cases with excellent fog detection using the 1:1 validation method were those with more than 300 fog pixels, indicating that the level of fog detection is excellent when the fog intensity is strong and the occurrence area is large. However, there was a high uncertainty and low detection level in T5 and T6 compared to other cases, regardless of the validation method (Figure 6a,b). In both cases, the total number of fog pixels was less than 100 (96 and 82), so the area where the fog occurred was narrow. T5 is a case where strong-intensity fog extended to the western coast and some areas of Seoul–Gyeonggi. T6 is a case where clouds and fog occurred together, making it difficult to detect the weak fog occurring between the clouds.

Among the validation cases, the fog detection levels were relatively high in the autumn cases (V7-9) and the spring cases (V2, V3) but low in the summer and winter cases (Figure 6c,d). Even in the validation case, fog cases with a high detection level had a low uncertainty. The detection level was highest in the V8 case, where radiation fog occurred extensively on land and clouds and fog were clearly distinguished on sea, regardless of the validation method. On the other hand, V10 showed the lowest POD and highest FAR values, resulting in the lowest detection level, followed by V6-V1-V12-V11. V10 is a case of very localized fog on land, showing the limitations in detecting localized fog despite using 500 m high-resolution data. Cases with low fog detection levels using the 1:1 validation method also tended to show low detection levels using the 1:9 validation method. However, in V12, although the fog detection level was very low using the 1:1 validation method, it showed a high fog detection level with a POD of 0.62 and FAR of 0.05 using the 1:9 validation method. In this case, a navigation error occurred in the satellite data, as presented in the discussion below.

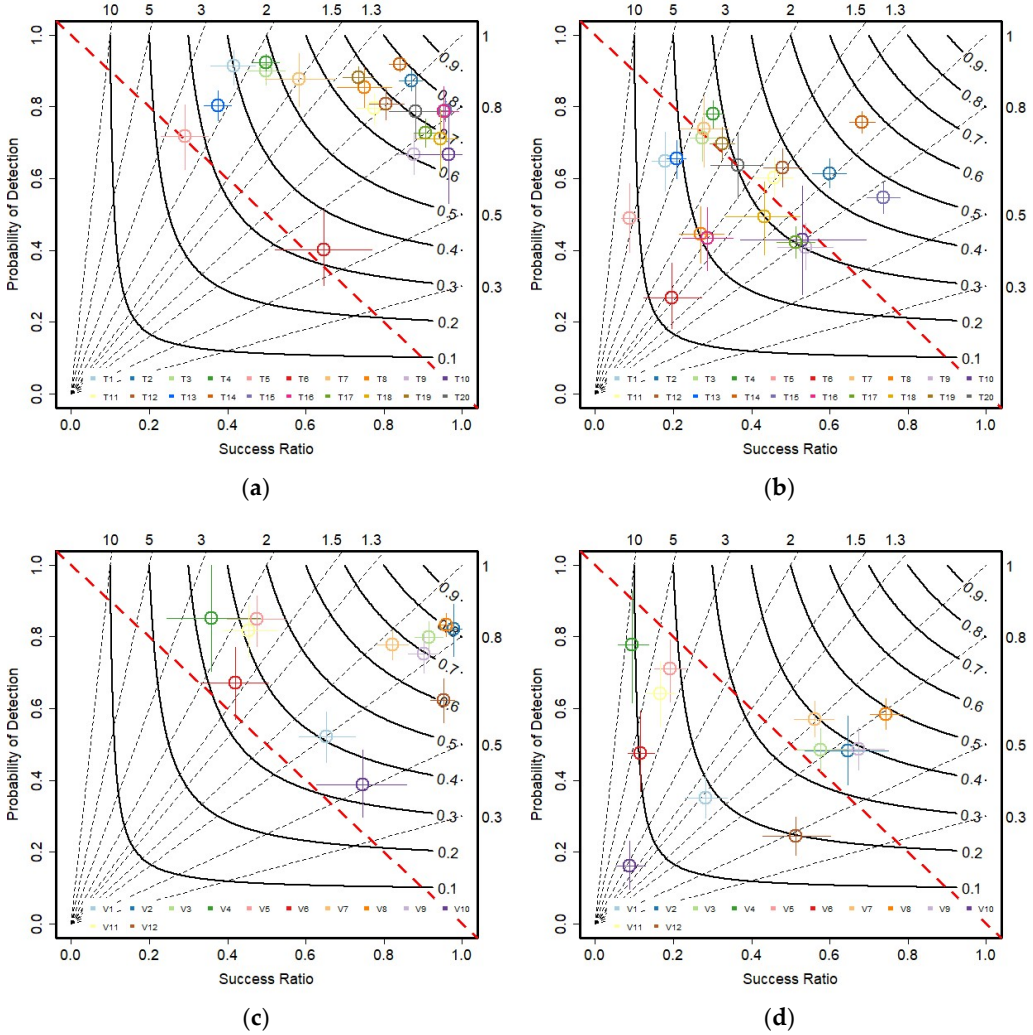

Figure 6. Performance diagram summarizing the Success Ratio (=1-FAR), POD, bias, and CSI for training (**a**,**b**) and validation (**c**,**d**) fog cases. The left (**a**,**c**) and right (**b**,**d**) diagrams show the 1:9 and 1:1 validation results, respectively. Dash and solid lines represent the bias scores and CSI, respectively. The sampling uncertainty is given by the crosshairs. The red line extending from top left to bottom right means that POD and FAR are the same value.

3.4. Comparison of Results between GK2A_FDA and GK2A_HR_FDA

Figure 7 is a graph comparing the fog detection levels of GK2A_FDA (2 km and 500 m fog products) developed by Han et al. [27] with those of GK2A_HR_FDA that was improved in this study. To objectively compare the fog detection levels of the three methods, we used 15 cases that overlap with the fog cases used by Han et al. [27]. To examine the fog detection levels according to the improvement in spatial resolution, fog products at a 500 m resolution using GK2A_FDA were produced and compared.

While there were differences depending on the fog case, the PODs of the three methods showed similar fog detection levels. However, it can be observed that the FAR of GK2A_HR_FDA decreased in all 15 cases. The average POD, FAR, and bias of GK2A_FDA (2 km resolution) were 0.80, 0.35, and 1.23, respectively, while GK2A_FDA (500 m resolution) showed values of 0.82, 0.40, and 1.37, indicating lower fog detection levels than those using a 2 km resolution. In other words, using GK2A_FDA to detect fog at a 500 m resolution leads to a higher false alarm rate, resulting in an over-detection of fog. GK2A_HR_FDA showed superior fog detection levels compared to GK2A_FDA, with an average POD, FAR, and bias of 0.81, 0.25, and 1.08, respectively. Moreover, the SD was lower in GK2A_HR_FDA than in GK2A_FDA for all statistical validation indices. Thus, the

fog detection level of GK2A_HR_FDA was improved compared to GK2A_FDA, regardless of the case. GK2A_HR_FDA is considered to have improved spatial resolution, resolved issues with over-detection, and enhanced stability compared to GK2A_FDA.

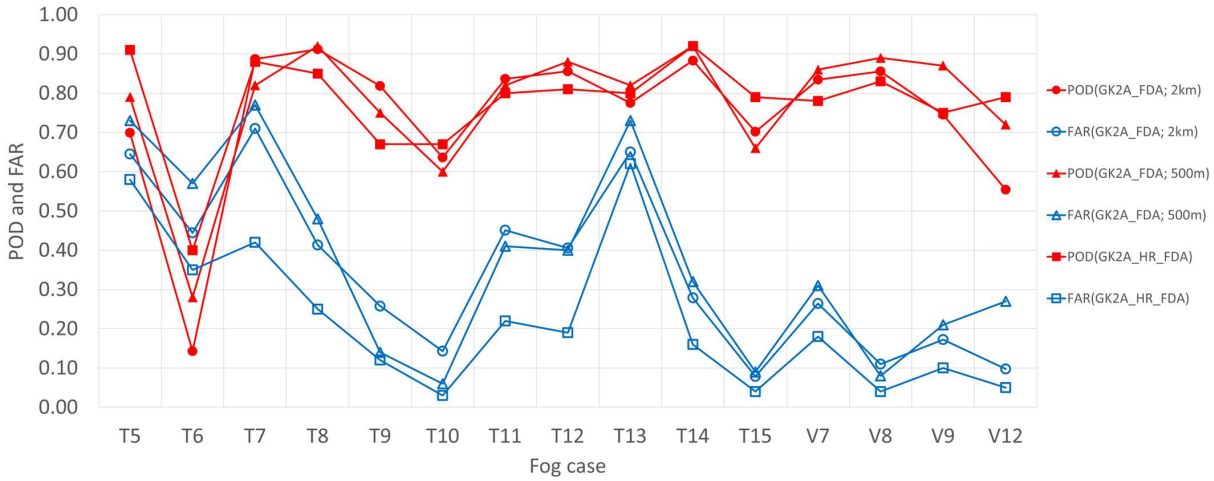

Figure 7. Comparison of fog detection level (POD, FAR) for the selected 15 fog cases based on the detection method (GK2A_FDA, GK2A_HR_FDA) and spatial resolution (2 km, 500 m). The T# and V# on the horizontal axis represent the fog cases used simultaneously in the GK2A_FDA and GK2A_HR_FDA of the cases presented in Table 2.

4. Discussion

The development and validation of GK2A_HR_FDA were conducted assuming that satellite navigation is accurate, the influence of cloud shadows is negligible, and the visibility data used for validation are accurate. Navigation errors in preprocessing by the NMSC are mostly negligible, within a few kilometers, but there are cases where significant navigation errors occur, as shown in Figure 8. If localized fog occurs during these times, errors in fog detection may arise due to differences between the background data and the satellite imagery. The impact will be especially significant in boundary areas with different land characteristics, such as coastal areas. After manual correction of navigation errors, the fog detection level was certainly improved, as shown in Table 7. Although this phenomenon does not occur frequently, it suggests the need for the automatic correction of navigation errors in operational fog detection.

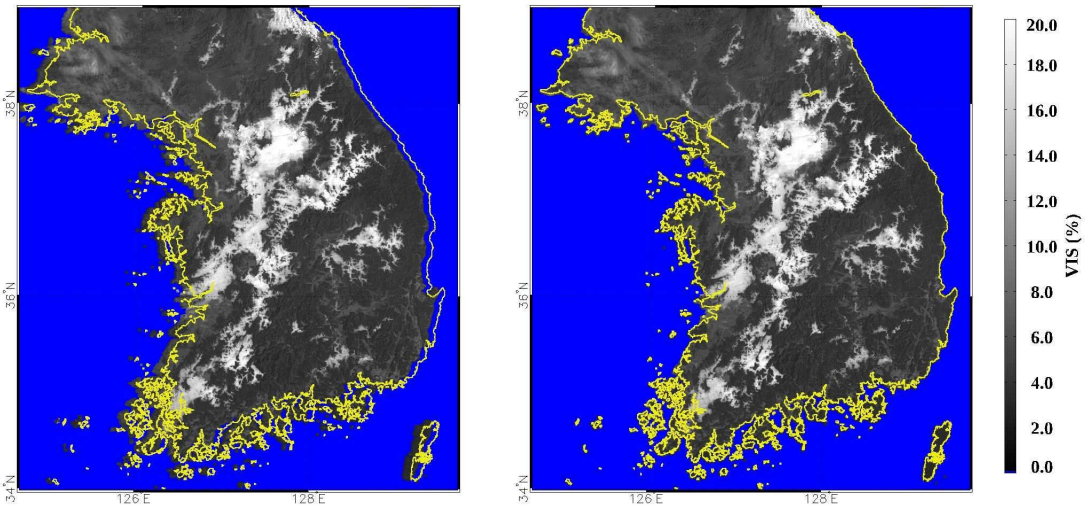

Figure 8. Samples of original image with a navigation error (**a**) and corrected image (**b**) at 09:00 KST on 6 November 2019. The sea is masked in blue.

Table 7. Validation results of fog detection before and after navigation error correction on 6 November 2019.

Validation Method	Status	POD	FAR	KSS	Bias	CSI
1:1 vali.	Before	0.21	0.18	0.02	0.26	0.20
	After	0.55	0.28	0.27	0.76	0.45
1:9 vali.	Before	0.39	0.13	0.27	0.45	0.37
	After	0.72	0.18	0.55	0.88	0.63

In this study, the reflectance background was derived using 30 days of mVC to minimize contamination from fog or clouds. However, if clouds occur during the day, shadows can occur on the ground (especially thick clouds at sunrise or sunset, which cause dark shadows). In addition, the composite period was 30 days, which does not adequately reflect the changes in and ground state and SZA that occur in spring and autumn. So, $Clr\_SFC\_R_{0.64}$ derived using mVC is lower than the actual value, leading to the over-detection of fog. Therefore, in this study, to minimize the influence of cloud shadows and the variation in SZA, the composite period was reduced from 30 days to 20 days. After changing the composite period, post-processing was added to remove the effects of clouds and cloud shadows. If the difference was greater (smaller) than the previous day's composite reflectance by 10%, it was considered to be contaminated with clouds (cloud shadows), so the composite reflectance of the previous day was used. Figure 9 illustrates the fog detection images of GK2A_HR_FDA before and after improving the reflectance background when cloud shadows occurred at 08 KST on 14 March 2021. In Figure 9a, it can be observed that the reflectance background near the east coast was significantly low due to cloud shadows, with contaminated pixels also visible over the sea. After improving the background reflectance, most of the cloud shadows were removed (Figure 9b). When fog was detected using the original reflectance background, it detected sea fog well along the west coast but over-detected fog over land (Figure 9c,e). After improving the reflection background, the problem of misclassifying clear pixels on land in the east coast region as fog was largely resolved (Figure 9d,e).

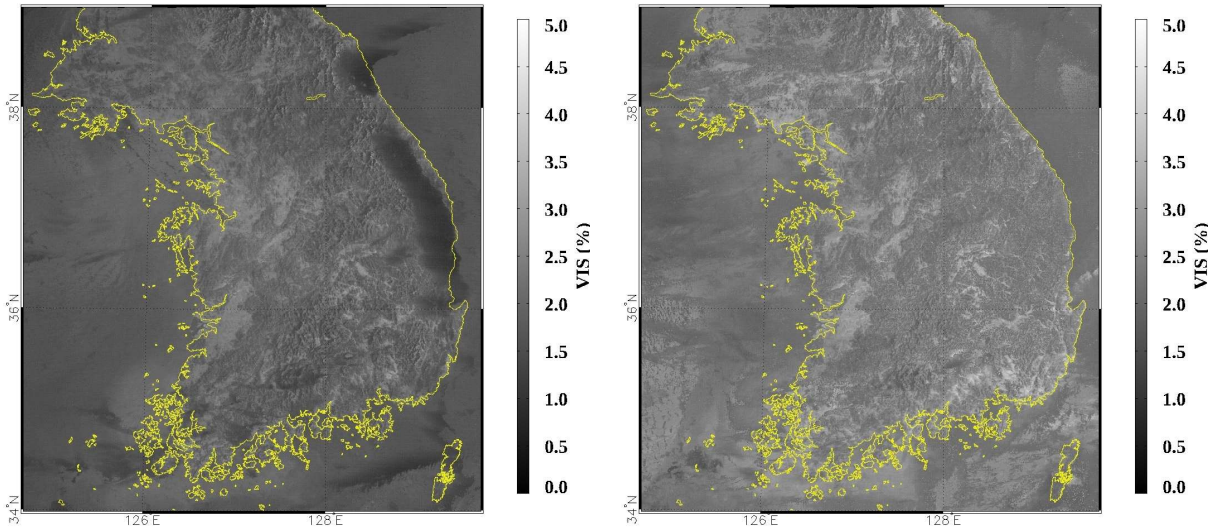

Figure 9. *Cont.*

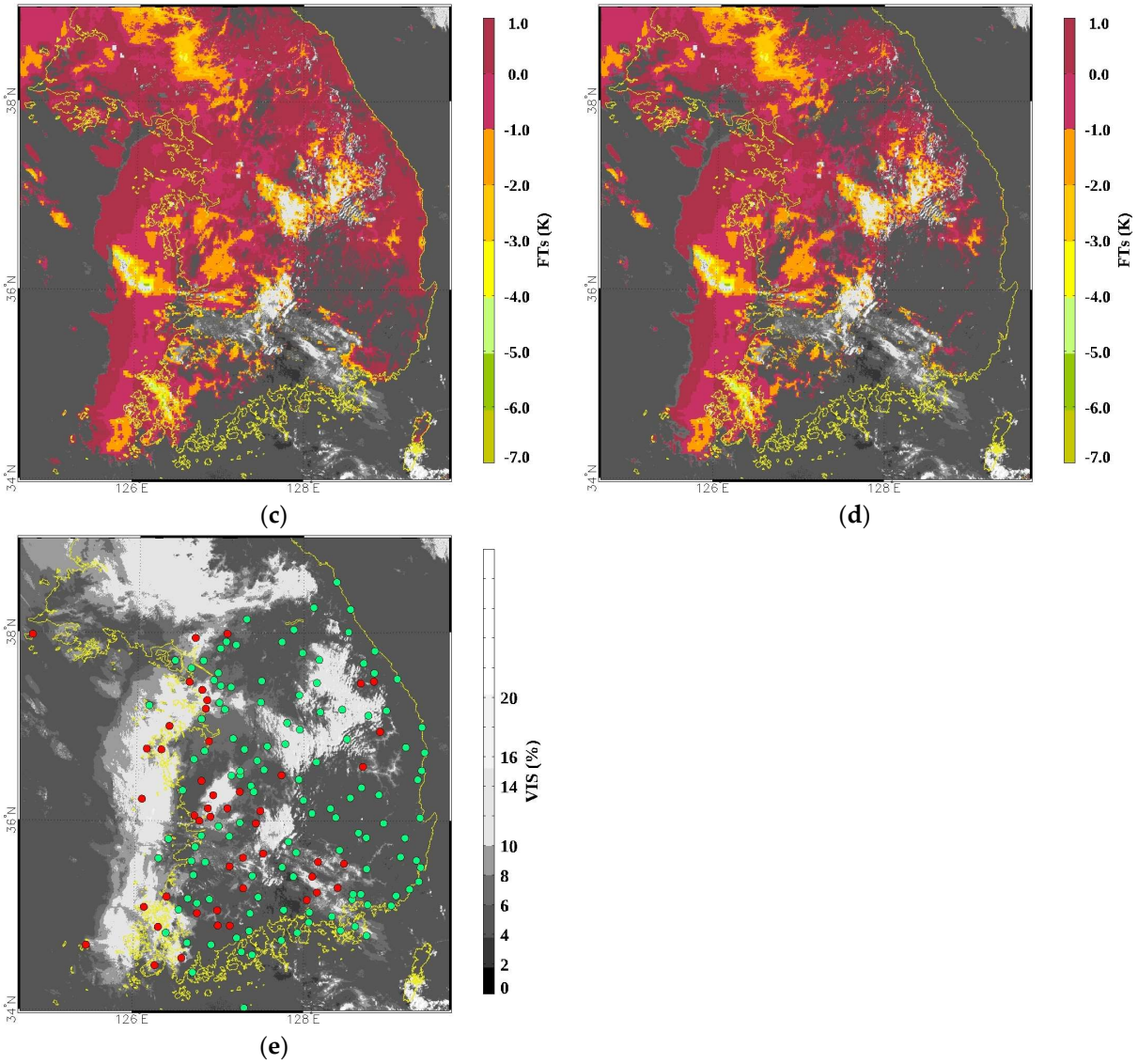

Figure 9. Examples of minimum value composited reflectance contaminated by the effects of cloud shadows (14 March 2021, 08:00 KST). (**a**) Reflection map produced using minimum value composition (mVC) for 30 days and (**b**) Reflectivity map generated by applying mVC and post-processing to 20-day data. (**c**,**d**) Images where fog was detected by applying the reflectivity map of (**a**) and (**b**), respectively. (**e**) Ground fog data with visible images of 0.64 um channel (red and green circles represent foggy and non-foggy area classified by visibility meter data, respectively).

Table 8 presents the fog detection levels before and after background improvement for 11 fog cases in 2021 where background improvement was possible (24 Jan., 7 Feb., 13 Feb., 5 Mar., 8 Mar., 14 Mar., 25 Mar., 6 Jun., 12 Jun., 19 Jun., 8 Dec.). Regardless of the validation method, the POD, FAR, and bias, on average, decreased after the background improvement. In particular, the bias significantly decreased from 2.14 to 1.93 (1:1 vali.) and from 2.20 to 2.00 (1:9 vali.). These results suggest that the accuracy of the background reflectance significantly influences the fog detection level of GK2A_HR_FDA.

Table 8. Comparison of the fog detection level in 11 fog cases before and after the improvement of the background field of reflectance through the elimination of cloud shadow effects.

Validation Method	Status	POD		FAR		KSS		Bias		CSI	
		Mean	SD	Mean	SD	Mean	SD	Mean	SD	Mean	SD
1:1 vali.	Before	0.62	0.16	0.71	0.16	−0.09	0.19	2.14	2.63	0.25	0.11
	After	0.60	0.15	0.69	0.17	−0.10	0.18	1.93	2.44	0.26	0.11
1:9 vali.	Before	0.76	0.12	0.65	0.23	0.11	0.18	2.20	2.61	0.31	0.16
	After	0.74	0.12	0.63	0.23	0.11	0.18	2.00	2.34	0.33	0.15

Although it was not analyzed in detail in this study, research is needed on the limitations of the spatial representativeness of the ground observation visibility data used for validation. Also, the Cloud-Aerosol Lidar and Infrared Pathfinder Satellite Observations (CALIPSO) are currently being used for the quantitative validation of sea fog [22,27,37]. However, since no CALIPSO data were available for the cases selected in this study, a quantitative comparison and validation of fog could not be performed. Therefore, there is a need for validation data for areas with limited quantitative validation data, especially over the sea.

5. Conclusions

In this study, to improve the fog detection level of the daytime fog detection algorithm using GK2A/AMI, three steps were performed: (1) increasing the fog detection resolution from 2 km to 500 m, (2) bias correction of the surface temperature predicted by the numerical model, and (3) optimization of the thresholds for test elements. Surface temperatures predicted by a numerical model were utilized to distinguish between fog and low-level clouds. Visibility and AWS/ASOS data were used for the quantitative validation of the fog detection level. A land–sea mask was used to consider different background properties in the fog detection process. To consider different fog occurrence characteristics depending on the season and geographical location, 32 fog cases were selected and classified into training cases (20) and validation cases (12) to develop a fog detection algorithm and validate the fog detection level.

The DBC method was developed to correct the prediction performance of numerical models depending on geographical location (land, sea, and coast) and time. This method dynamically adjusts according to the geographical location and time. Also, to improve the limitations of visibility data, relatively high-accuracy airport observation data were added and the RH and WS data of AWS/ASOS were used.

The systemic negative bias of the model was resolved regardless of the geographical location, time, and case by DBC. After DBC application and threshold value adjustment, FAR (−0.02–−0.06) and bias (−0.07–−0.23) decreased, but CSI (+0.01–+0.03) increased in both the training and validation cases. GK2A_HR_FDA, with improved spatial resolution, not only improved local fog detection levels, but also partially alleviated the over-detection problems. The variability (standard deviation) of each validation index also decreased. Considering that the 32 cases used in this study consisted of a total of 2304 sets (32 cases × 6 sets/h × approximately 12 h (daytime = approximately 2304 sets)), these results suggest that the fog detection performance and stability of GK2A_HR_FDA were improved.

The level of fog detection was very low in some fog cases due to unusually large navigation errors and errors in the reflectance background field caused by cloud shadows. After the correction of navigation errors and the cloud shadow effect, the fog detection level was certainly improved. In particular, the bias significantly decreased from 2.14 to 1.93 (1:1 vali.) and from 2.20 to 2.00 (1:9 vali.). Therefore, to improve the localized fog detection level, it is necessary to develop automated and detailed correction techniques for navigation errors and cloud shadow effects. In addition to that, to reduce the high false detection rate and variability of fog detection algorithms on the coast, regardless of the limited number of coastal pixels and validation cases, the further sophistication of daytime fog detection algorithms is needed.

Author Contributions: Conceptualization, M.-S.S.; methodology, M.-S.S. and J.-H.H.; software, J.-H.H. and H.-Y.Y.; validation, J.-H.H.; formal analysis, J.-H.H., M.-S.S. and H.-Y.Y.; investigation, J.-H.H., H.-Y.Y. and S.-H.K.; resources, M.-S.S.; data curation, J.-H.H., H.-Y.Y. and S.-H.K.; writing—original draft preparation, J.-H.H.; writing—review and editing, M.-S.S.; visualization, J.-H.H. and H.-Y.Y.; supervision, M.-S.S.; project administration, M.-S.S.; funding acquisition, M.-S.S. All authors have read and agreed to the published version of the manuscript.

Funding: This research was supported by the Specialized university program for confluence analysis of Weather and Climate Data of the Korea Meteorological Institute (KMI) funded by the Korean government (KMA).

Data Availability Statement: Data from GK2A/AMI are freely available to registered users on the NMSC/KMA web portal: https://datasvc.nmsc.kma.go.kr/datasvc/html/main/main.do?lang=en accessed on 31 January 2023. The visibility and AWS data are available from the KMA API Hub (https://apihub.kma.go.kr/) accessed on 31 January 2023. Numerical model data used in this study can be obtained upon request to the NMSC/KMA.

Acknowledgments: We are also grateful to the Korean Meteorological Administration's National Meteorological Satellite Center for providing vast amounts of satellite and numerical data.

Conflicts of Interest: The authors declare no conflicts of interest.

References

1. Gultepe, I.; Tardif, R.; Michaelides, S.C.; Cermak, J.; Bott, A.; Bendix, J.; Müller, M.D.; Pagowski, M.; Hansen, B.; Ellrod, G.; et al. Fog Research: A Review of Past Achievements and Future Perspectives. *Pure Appl. Geophys.* **2007**, *164*, 1121. [CrossRef]
2. Cermak, J.; Eastman, R.M.; Bendix, J.; Warren, S.G. European Climatology of Fog and Low Stratus Based on Geostationary Satellite Observations. *Q. J. R. Meteorol. Soc.* **2009**, *135*, 2125. [CrossRef]
3. Egli, S.; Thies, B.; Bendix, J. A Hybrid Approach for Fog Retrieval Based on a Combination of Satellite and Ground Truth Data. *Remote Sens.* **2018**, *10*, 628. [CrossRef]
4. Guo, X.; Wan, J.; Liu, S.; Xu, M.; Sheng, H.; Yasir, M. A scSE-LinkNet Deep Learning Model for Daytime Sea Fog Detection. *Remote Sens.* **2021**, *13*, 5136. [CrossRef]
5. Yi, L.; Li, M.; Liu, S.; Shi, X.; Li, K.; Bendix, J. Detection of Dawn Sea Fog/Low Stratus using Geostationary Satellite Imagery. *Remote Sens. Environ.* **2023**, *294*, 113622. [CrossRef]
6. Shin, D.G.; Kim, J.H. A New Application of Unsupervised Learning to Nighttime Sea Fog Detection. *Asia-Pac. J. Atmos. Sci.* **2018**, *54*, 527. [CrossRef]
7. Tardif, R.; Rasmussen, R.M. Event-Based Climatology and Typology of Fog in the New York City Region. *J. Appl. Meteorol. Climatol.* **2006**, *46*, 1141. [CrossRef]
8. Lee, H.D.; Ahn, J.B. Study on classification of fog type based on its generation mechanism and fog predictability using empirical method. *Atmosphere* **2013**, *23*, 103–112. [CrossRef]
9. Akimoto, Y.; Kusaka, H. A Climatological Study of Fog in Japan Based on Event Data. *Atmos. Res.* **2014**, *151*, 200. [CrossRef]
10. Lee, H.K.; Suh, M.S. A comparative study on the visibility characteristics of naked-eye observation and visibility meters of fog over South Korea. *Atmosphere* **2018**, *28*, 69–83. [CrossRef]
11. Lee, Y.H.; Lee, J.S.; Park, S.K.; Chang, D.E.; Lee, H.S. Temporal and Spatial Characteristics of Fog Occurrence Over the Korean Peninsula. *J. Geophys. Res.* **2010**, *115*, D14117. [CrossRef]
12. Park, H.M.; Kim, J.H. Detection of sea fog by combining MTSAT infrared and AMSR microwave measurements around the Korean Peninsula. *Atmosphere* **2012**, *22*, 163–174. [CrossRef]
13. Oh, Y.J.; Suh, M.S. Development of quality control method for visibility data based on the characteristics of visibility data. *Korean J. Remote Sens.* **2020**, *36*, 707–723. [CrossRef]
14. Eyre, J.R.; Brownscombe, J.L.; Allam, R.J. Detection of fog at night using Advanced Very High Resolution Radiometer (AVHRR) imagery. *Meteorol. Mag.* **1984**, *113*, 266–271.
15. Anthis, A.I.; Cracknell, A.P. Use of satellite images for fog detection (AVHRR) and forecast of fog dissipation (METEOSAT) over lowland Thessalia, Hellas. *Int. J. Remote Sens.* **1999**, *20*, 1107–1124. [CrossRef]
16. Bendix, J.; Thies, B.; Nauß, T.; Cermak, J. A Feasibility Study of Daytime Fog and Low Stratus Detection with TERRA/AQUA-MODIS Over Land. *Meteorol. Appl.* **2006**, *13*, 111. [CrossRef]
17. Shang, H.; Chen, L.; Letu, H.; Zhao, M.; Li, S.; Bao, S. Development of a daytime cloud and haze detection algorithm for Himawari-8 satellite measurements over central and eastern China. *Geophys. Res. Atmos.* **2017**, *122*, 3528–3543. [CrossRef]
18. Cermak, J. SOFOS—A New Satellite-Based Operational Fog Observation Scheme. Ph.D. Thesis, Phillipps-University, Marburg, Germany, 2006.
19. Gultepe, I.; Pagowski, M.; Reid, J. A satellite-based fog detection scheme using screen air temperature. *Weather. Forecast.* **2007**, *22*, 444–456. [CrossRef]

20. Musial, J.P.; Hüsler, F.; Sütterlin, M.; Neuhaus, C.; Wunderle, S. Daytime low stratiform cloud detection on AVHRR imagery. *Remote Sens.* **2014**, *6*, 5124–5150. [CrossRef]
21. Weston, M.; Temimi, M. Application of a nighttime fog detection method using SEVIRI over an arid environment. *Remote Sens.* **2020**, *12*, 2281. [CrossRef]
22. Shin, D.G.; Park, H.M.; Kim, J.H. Analysis of the fog detection algorithm of DCD method with SST and CALIPSO data. *Atmosphere* **2013**, *23*, 471–483. [CrossRef]
23. Suh, M.S.; Lee, S.J.; Kim, S.H.; Han, J.H.; Seo, E.K. Development of land fog detection algorithm based on the optical and textural properties of fog using COMS data. *Korean J. Remote Sens.* **2017**, *33*, 359–375. [CrossRef]
24. Han, J.H.; Suh, M.S.; Kim, S.H. Development of day fog detection algorithm based on the optical and textural characteristics using Himawari-8 data. *Korean J. Remote Sens.* **2019**, *35*, 117–136. [CrossRef]
25. Kim, S.H.; Suh, M.S.; Han, J.H. Development of fog detection algorithm during nighttime using Himawari-8/AHI satellite and ground observation data. *Asia-Pac. J. Atmospheric Sci.* **2019**, *55*, 337–350. [CrossRef]
26. Ryu, H.S.; Hong, S. Sea fog detection based on Normalized Difference Snow Index using advanced Himawari imager observations. *Remote Sens.* **2020**, *12*, 1521. [CrossRef]
27. Han, J.H.; Suh, M.S.; Yu, H.Y.; Roh, N.Y. Development of fog detection algorithm using GK2A/AMI and ground data. *Remote Sens.* **2020**, *12*, 3181. [CrossRef]
28. Yu, H.Y.; Suh, M.S. Development of High-Resolution Fog Detection Algorithm for Daytime by Fusing GK2A/AMI and GK2B/GOCI-II Data. *Korean J. Remote Sens.* **2023**, *39*, 1779–1790. [CrossRef]
29. Chung, S.R.; Ahn, M.H.; Han, K.S.; Lee, K.T.; Shin, D.B. Meteorological products of Geo-KOMPSAT 2A (GK2A) satellite. *Asia-Pac. J. Atmos. Sci.* **2020**, *56*, 185. [CrossRef]
30. Lee, H.B.; Heo, J.H.; Sohn, E.H. Korean fog probability retrieval using remote sensing combined with machine-learning. *GISci. Remote Sens.* **2021**, *58*, 1434–1457. [CrossRef]
31. Piani, C.; Weedon, G.P.; Best, M.; Gomes, S.M.; Viterbo, P.; Hagemann, S.; Haerter, J.O. Statistical bias correction of global simulated daily precipitation and temperature for the application of hydrological models. *J. Hydrol.* **2010**, *395*, 199–215. [CrossRef]
32. Durai, V.R.; Bhradwaj, R. Evaluation of statistical bias correction methods for numerical weather prediction model forecasts of maximum and minimum temperatures. *Nat. Hazards* **2014**, *73*, 1229–1254. [CrossRef]
33. Jung, H.C.; Suh, M.S. Correction of mean and extreme temperature simulation over south Korea using a trend-preserving bias correction method. *Atmosphere* **2015**, *25*, 205–219. [CrossRef]
34. Kang, T.H.; Suh, M.S. Detailed Characteristics of Fog Occurrence in South Korea by Geographic Location and Season—Based on the Recent Three Years (2016–2018) Visibility Data. *J. Clim. Res.* **2019**, *14*, 221–244. [CrossRef]
35. Lee, H.K.; Suh, M.S. Objective classification of fog type and analysis of fog characteristics using visibility meter and satellite observation data over South Korea. *Atmosphere* **2019**, *29*, 639–658. [CrossRef]
36. Kim, E.J.; Park, S.Y.; Yoo, J.W.; Lee, S.H. Fog type classification and occurrence characteristics based on fog generation mechanism in Korea Peninsula. *J. Environ. Sci. Int.* **2023**, *32*, 883–898. [CrossRef]
37. Wu, D.; Lu, B.; Zhang, T.; Yan, F. A method of detecting sea fogs using CALIOP data and its application to improve MODIS-based sea fog detection. *J. Quant. Spectrosc. Radiat. Transf.* **2015**, *153*, 88–94. [CrossRef]